


Stabilization of *A*-site ordered perovskites and formation of spin-half antiferromagnetic lattice: $\text{CaCu}_3\text{Ti}_4\text{O}_{12}$ and $\text{CaCu}_3\text{Zr}_4\text{O}_{12}$

Jatin Kumar Bidika,^{*} Amit Chauhan,^{*} and B. R. K. Nanda[†]

Condensed Matter Theory and Computational Lab, Department of Physics, Indian Institute of Technology Madras, Chennai 600036, India;
Center for Atomistic Modelling and Materials Design, Indian Institute of Technology Madras, Chennai 600036, India;
and Functional Oxide Research Group, Indian Institute of Technology Madras, Chennai 600036, India

 (Received 8 March 2022; revised 12 July 2022; accepted 16 September 2022; published 30 September 2022)

A-site ordered perovskites, $\text{CaCu}_3\text{B}_4\text{O}_{12}$, which are derivatives of conventional ABO_3 perovskites, exhibit varying electronic and magnetic properties. With the objective of examining the role of Cu in this work, we have studied $\text{CaCu}_3\text{Ti}_4\text{O}_{12}$ and $\text{CaCu}_3\text{Zr}_4\text{O}_{12}$ and presented the cause of the crystallization of *A*-site ordered perovskite from conventional ABO_3 perovskite and the underlying mechanism leading to the stabilization of nontrivial and experimentally established *G*-type antiferromagnetic (*G*-AFM) ordering in these systems. The first-principles electronic structure calculations supplemented with phonon studies show that the formation of *A*-site ordered perovskite is driven by Jahn-Teller distortion of the CuO_{12} icosahedron. The crystal orbital Hamiltonian population analysis and magnetic exchange interactions estimated using spin dimer analysis infer that the nearest and next-nearest-neighbor interactions (J_1 and J_2) are direct and weakly ferromagnetic, whereas the third-neighbor interaction (J_3) is unusually strong and antiferromagnetic driven by an indirect superexchange mechanism. The structural geometry reveals that stabilization of *G*-AFM requires $J_1 < 2J_2$, $J_1 < 2J_3$. The experimental and theoretical values of Néel temperature agree well for $U \approx 7$ eV, highlighting the role of strong correlation. The magnetic ordering is found to be robust against pressure and strain.

DOI: [10.1103/PhysRevB.106.115152](https://doi.org/10.1103/PhysRevB.106.115152)

I. INTRODUCTION

In the past several decades, perovskite transition-metal oxides with the formula ABO_3 have been studied extensively as these pristine compounds and their derivatives facilitate a plethora of intriguing electronic and magnetic properties both for fundamental studies and novel applications [1–4]. These properties can be tuned by applying external pressure or strain, electric and magnetic fields, or by changing the chemical composition [5–9]. Here *A* is either a rare-earth element or alkaline-earth metal, and *B* is a transition-metal atom.

Another class of perovskites, known as quadruple perovskites or *A*-site ordered perovskites, is less explored despite having equally intriguing electronic structure [10,11]. This family of perovskites with the chemical formula $\text{AA}'_3\text{B}_4\text{O}_{12}$ are derived from the cubic perovskite structure in which *A*- and *A'*-site cations form an ordered structure with 1:3 composition. While *A* is an alkaline earth metal, *A'* belongs to a transition-metal atom. The $\text{CaCu}_3\text{Ti}_4\text{O}_{12}$ (CCTiO) is an antiferromagnetic insulator and possesses Néel temperature (T_N) of ≈ 25 K and a giant dielectric constant of the order 10^4 over a wide range of temperature [12–16]. Furthermore, the x-ray absorption spectroscopy measurements confirm the antiferromagnetic ordering of CCTiO [17]. The manganate, $\text{CaCu}_3\text{Mn}_4\text{O}_{12}$, exhibits colossal magnetoresistance even under a lower magnetic field due to Mn^{4+} character

[18]. The high-temperature phase of $\text{CaCu}_3\text{Fe}_4\text{O}_{12}$ exhibits a ferrimagnetic ground state where Fe is in a homogeneous valence state (Fe^{4+}) whereas the low-temperature phase shows charge disproportionation from Fe^{4+} to Fe^{5+} [19]. The Zhang-Rice singlet state was observed in the ferromagnetic metal $\text{CaCu}_3\text{Co}_4\text{O}_{12}$ and ferromagnetic half-metal $\text{CaCu}_3\text{Ni}_4\text{O}_{12}$ [20,21]. The candidates of the CCBO family with *B*-site as *4d* transition-metal elements $\text{CaCu}_3\text{Ru}_4\text{O}_{12}$ and $\text{CaCu}_3\text{Rh}_4\text{O}_{12}$ exhibit a Pauli paramagnetic metallic state [22–24]. The CCRuO is a heavy-fermionic system where Cu and Ru possess 2+ and 4+ oxidation states, whereas in CCRhO, the unusual oxidation states $\approx 2.8+$ and $3.4+$ were attributed to the larger crystal-field splitting.

There are two issues that need to be addressed to understand and tailor the fundamental phenomena involving the couplings of spin, charge, and lattice degrees of freedom in CCBO. First, the empirical observations suggest that the *B*-site hardly influences the crystallization in the quadruple perovskite structure, and therefore the role of Cu in achieving structural stability should be explained. The second issue involves the magnetic ordering when the *B*-site is magnetically inactive and composed of *sp*-elements. For example, $\text{CaCu}_3\text{Ge}_4\text{O}_{12}$ and $\text{CaCu}_3\text{Sn}_4\text{O}_{12}$ systems are found to be fully ferromagnetic [25]. However, if the *B*-site is magnetically inactive but composed of *d*-elements, as in the case of CCTiO, CCZrO, and $\text{CaCu}_3\text{Pt}_4\text{O}_{12}$, the system stabilizes in an unnatural antiferromagnetic state [11,26]. One of the theoretical studies on CCTiO/CCZrO by Toyoda *et al.* suggests that the nearest-neighbor Cu spins prefer weak ferromagnetic coupling while the third-neighbor Cu spins favor strong antiferromagnetic coupling in these spin-half lattices [26].

^{*}These authors contributed equally to this work.

[†]nandab@iitm.ac.in

The ferromagnetic coupling was explained through the indirect exchange interaction via the Cu-O-Cu path, whereas the strong antiferromagnetic coupling was explained through superexchange interaction via a zigzag Cu-O-Ti-O-Cu path. Furthermore, the estimated value of Néel temperature was quite high (≈ 70 K) as compared to the experimentally observed value of 25 K. Contrary to Toyoda *et al.*, Lacroix [27] considered the exchange paths that exclude the oxygen atoms (Cu-Ti-Cu interaction) to explain the ground-state magnetic configuration. Therefore, the mechanism of magnetic couplings is still unsettled.

To address the aforementioned issues, we have investigated the experimentally synthesized CCTiO [28,29] and yet to be synthesized CCZrO with the aid of density functional theory (DFT) calculations. The d^0 configuration of Ti and Zr provides a Cu-only spin lattice and makes the Fermi level devoid of any B-site electrons. This implies that the Cu is responsible both for the magnetization as well as the symmetry-lowered crystallization of these compounds. Furthermore, the present study provides insight on the effect of strong correlation on the magnetic structure of these systems, which is missing in the literature. Also, in correlated oxide systems, often strain and pressure are employed to induce a magnetic transition. In this work, we have examined whether such a transition can be achieved here as well. To establish the mechanism of magnetic exchange interactions, the electron hopping integrals involving the orbitals of various atom pairs (Cu-O, Cu-Ti, Cu-Cu, etc.) in different exchange paths are analyzed using a projected crystal orbital Hamilton population (pCOHP). The strength of exchange interactions is obtained by employing spin dimer analysis.

From electronic structure analysis, we find that the structural transition from cubic to A-site ordered structure is driven by Jahn-Teller distortion of the Cu-O complex. The distortion is necessary to lower the density of degenerate states at the Fermi level. The analysis of exchange interaction infers that the nearest and next-nearest neighbor (J_1 and J_2) interactions are direct and hence weakly ferromagnetic. However, the third-neighbor (J_3) interaction is found to be relatively stronger and antiferromagnetic, driven by a long-range superexchange mechanism leading to the formation of G-type antiferromagnetic ordering. The exchange pathways are validated through COHP analysis. The exact match between the experimentally observed value of T_N (≈ 25 K) is found for $U \approx 7$ eV, signifying the importance of electron correlation in this family of compounds. The revised exchange interaction mechanisms in this present study will pave the way to reexamine the electronic and magnetic structure of other members of this A-site ordered perovskite family.

II. STRUCTURAL AND COMPUTATIONAL DETAILS

The regular perovskite (ABO_3) structure is shown in Fig. 1(a). Had the CCBO stabilized in this structure, Ca and Cu would have shared the A site. The stable A-site ordered perovskite configuration is shown in Fig. 1(b). It contains two formula units per unit cell. The B-site transition-metal elements form BO_6 distorted octahedral complexes, whereas the A-site doped Cu atoms form square planar CuO_4 complexes in the xy , yz , and xz planes. Each distorted octahedral

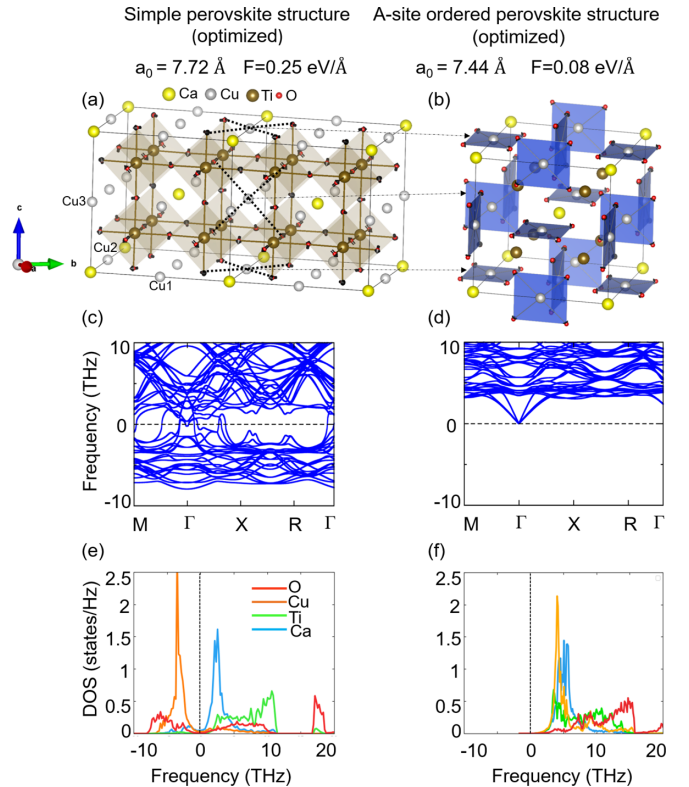


FIG. 1. (a) The hypothetical volume-optimized structure of CC-TiO modeled based on single perovskite structure (ABO_3). In this eight-formula unit cell, six of the A (Ca) atoms are replaced by Cu atoms to form the stoichiometry $CaCu_3Ti_4O_{12}$. The octahedra (OH) and square planar (SP) complexes are shown. The force (F) at the atomic sites is mapped to give an insight on the possible displacement of anions leading to intra- and interdistortion of the OH and SP complexes. (b) The stable crystal structure as obtained from experiment. Parts (c),(d) and (e),(f), respectively, display the phonon band structures and atom-resolved density of states corresponding to the cubic and experimental structure.

complex is interlocked with the six square planar complexes. The distortion of the regular perovskite leading to the A-site ordered perovskite structure is discussed later.

The first-principles based electronic-structure calculations are performed using the full-potential linearized augmented plane wave (FP-LAPW) [30] method as implemented in the WIEN2K [31] code. For all calculations, the generalized gradient approximation (GGA) was considered for the exchange-correlation functional. An $8 \times 8 \times 8$ k -mesh was used for the Brillouin zone integration and is found to be sufficient to estimate the electronic structure with reasonable accuracy. The mean-field based parametric Hubbard U formalism is adopted to examine the effect of on-site Coulomb repulsion giving rise to strong correlation. It is done through the rotationally invariant Dudarev approach with $U_{\text{eff}} = U - J$ [32,33], where U and J are Hubbard and Hund's exchange parameters, respectively. Herein, the value of J is considered to be zero. Therefore, the U_{eff} becomes U . The convergence criterion for the total energy and charge density was set as 10^{-4} Ry. The electronic-structure calculations were performed using both experimental and optimized lattice

TABLE I. The B site transition-metal element in the CCBO system, optimized and experimental lattice parameter a in (Å). The M-O and Cu-O bond lengths are in (Å); O-B-O, O-Cu-O, B-O-B, and Cu-O-B bond angles are listed for the CCBO system.

CCBO	a	B-O	Cu-O	O-Cu-O	O-B-O	B-O-B	Cu-O-B
CCTiO (optimized)	7.448	1.98	1.96	96.34°, 83.66°	89.02°, 90.98°	139.89°	109.57°
CCTiO (experiment)	7.391	1.97	1.94	90.69°, 89.31°	87.09°, 92.91°	139.94°	110.02°
CCZrO (optimized)	7.887	2.13	2.00	81.33°, 98.66°	88.57°, 91.42°	135.22°	111.58°

parameters for CCTiO and the optimized lattice parameter for CCZrO. First we performed the spin-polarized calculations within GGA, and then we considered the Coulomb interaction through GGA+ U calculations. The density functional perturbation theory (DFPT) [34,35] approach is adopted for the phonon calculations without considering the U . The force constants obtained from the DFPT method are taken into account through the PHONOPY code as implemented in the Vienna ab-initio Simulation Package (VASP) [36,37]. For the phonon calculations, a $1 \times 1 \times 2$ supercell is considered.

To understand the nature of the mechanism for the exchange paths, the pCOHP is calculated for different atom pairs. The pCOHP is a partitioning of the band-structure energy in terms of orbital-pair contributions. In principle, the pCOHP indicates bonding and antibonding energy regions for a specified energy range. The pCOHP is expressed as

$$\text{pCOHP}_{\mu,\nu}(E, k) = \sum_j R[P_{\mu\nu j}^{\text{proj}}(k)H_{\nu\mu}^{\text{proj}}(k)] \times \delta(\epsilon_j(k) - E), \quad (1)$$

where $P_{\mu\nu j}^{\text{proj}}(k)$ is the projected density matrix for band j at the k -point, and $H_{\nu\mu}$ is the hybridization strength of orbital pairs μ and ν centered at two atoms. The pCOHP calculations were performed by using the local-orbital basis suit towards electronic-structure reconstruction (LOBSTER) code [38,39].

The optimized lattice parameters, the B-O and Cu-O bond lengths, the local and global O-B-O, O-Cu-O, B-O-B, and Cu-O-B bond angles, along with the experimental lattice parameters [11,12] of the CCTiO and CCZrO are given in Table I.

III. RESULTS AND DISCUSSION

A. Formation of the A-site ordered perovskite structure:

Role of Cu- d electrons

In the conventional single perovskite oxides ABO_3 , B forms a BO_6 octahedron while A forms an AO_{12} icosahedron. This structure is stable when A is an electron donor from the alkali/alkaline or rare-earth family and does not participate in covalent bonding to form the band structure. However, when a transition-metal element such as Cu occupies the A sites, as shown in Fig. 1(a), the phonon band structures yield a large number of imaginary frequencies [see Fig. 1(c)] indicating huge instability for the simple perovskite structure of $\text{CaCu}_3\text{Ti}_4\text{O}_{12}$. This hypothetical perovskite structure is built by considering an eight-formula unit CaTiO_3 cell and replacing six of the Ca by Cu. While there are many possible arrangements of Ca and Cu that can be thought of in this hypothetical structure, they are broadly put together into two groups, one in which the Ca cations are close to each other, and the other case when they are away from each other. Our

total energy calculations suggest that the former is unstable compared to the latter by ~ 3.3 eV. Therefore, the minimum energy configuration is built by keeping the Ca ions away from each other, as shown in Fig. 1(a).

Now we shall further analyze the phonon spectra to establish the stabilization of the A-site ordered perovskite structure out of the simple ABO_3 structure. In Fig. 1(e), we have plotted the site projected phonon DOS for the latter, and it shows that the dominant contribution to these imaginary frequencies comes from the Cu and O sites, whereas the Ca sites have a very nominal contribution, which infers the negligible role of Ca towards structural instability. The presence of dominant imaginary frequencies is attributed to the large electrostatic force exerted among the Cu cation and O anions in the Cu-O icosahedron. As a consequence, the system undergoes a symmetry-lowering structural transition. The force driving this transition is indicated in Fig. 1(a), and the resultant displacement leading to the formation of square-planar complexes is indicated using dashed lines. The ionic displacements by the lighter O atoms lead to the formation of A-site ordered structure [Fig. 1(b)]. The dynamical stability of this structure is inferred from the absence of imaginary frequencies [Figs. 1(d) and 1(f)]. The primary understanding towards the stabilization of the A-site ordered perovskite structure out of a simple cubic perovskite structure can be obtained by examining the electronic structure of the system. According to the Jahn-Teller theorem [40], if there are degenerate states occupying the Fermi level (E_F), the cation-anion complexes distort to reduce the covalent interaction and in turn to deplete the degenerate density of states (DOS) at the E_F [41]. This results in a reduction of kinetic energy and stabilization of the structure. Interestingly, depletion of the DOS at E_F can also occur through spin polarization, which is well understood through the Stoner criterion. Through Fig. 2, where the band structure and DOS are plotted, we examine the role of symmetry breaking on the electronic structure and magnetization of CCTiO. The top and bottom rows represent the case of simple perovskite and A-site order perovskite structure (experimental), respectively. The results for the nonmagnetic (NM), ferromagnetic (FM), and G -type antiferromagnetic (G -AFM) states are presented columnwise. The nonmagnetic configuration in the simple perovskite structure shows a large DOS at E_F with a large number of degenerate bands. Since the Ti $4+$ charge state leads to a d^0 electronic configuration, these degenerate bands arise solely from the Cu- d states.

The Cu at A-site creates an icosahedron that can be viewed as three superimposing square-planar complexes lying on the xy , yz , and xz planes (see the inset in the top row of Fig. 2). Therefore, the net effective crystal field is the sum of the three independent square planar crystal fields, and as a result the otherwise nondegenerate crystal-field-split orbitals overlap to

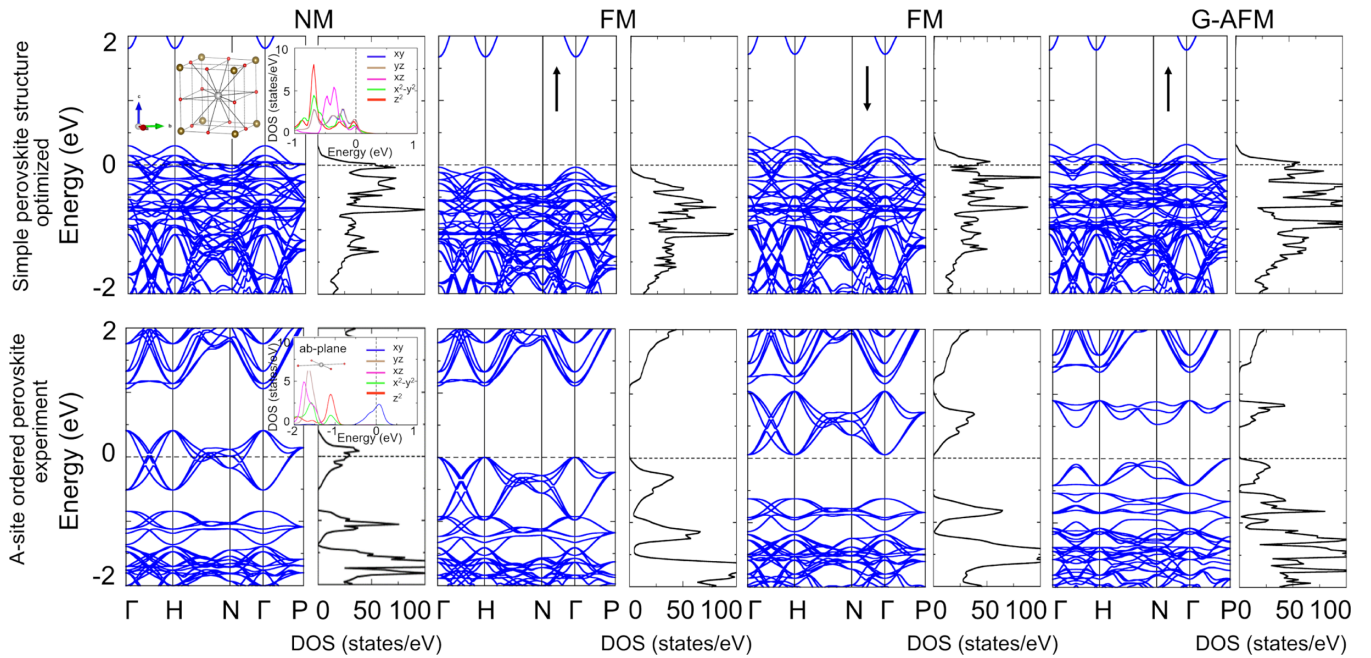


FIG. 2. Electronic structure, as represented through bands and DOS, for nonmagnetic, ferromagnetic, and G -type antiferromagnetic states for an optimized simple perovskite structure (top row), and experimental A -site ordered perovskite (bottom row). For the NM simple perovskite structure, even though the Cu1- d states experience an icosahedron crystal field, the xz DOS differs from the xy and yz DOS. This is due to the fact that the Cu1-O-Cu2 and Cu1-O-Cu3 chains are periodic in the ab and bc planes, which allows a continuous d - p - d electron hopping. However, in the ac plane this hopping path is broken due to the presence of the Cu1-O-Ca-O-Cu1 chain, and as a result the xz DOS differs from the degenerate xy and yz DOS. Similar inferences can be made for Cu2- yz and Cu3- xy orbitals.

form a new set of degenerate states occupying E_F . As a consequence, the states in the vicinity of E_F are highly degenerate. Since the conventional unit cell consists of six equivalent Cu atoms, there are 30 spin-degenerate d -orbitals and the partial DOS indicates that 18 of them cross the E_F . These degenerate states bring Jahn-Teller instability, and therefore the lattice undergoes distortion to give rise to isolated square planar complexes as discussed in the previous paragraph. In the square-planar crystal field, the fivefold-degenerate d -orbitals split into four manifolds with three nondegenerate states and one twofold-degenerate state as demonstrated in the inset of the bottom row of Fig. 2. From each complex, only one non-degenerate d -state crosses E_F , and hence altogether there are only 6 bands instead of 18. A filled shell electronic structure of the Ca^{2+} ion does not contribute to the JT distortion.

While the Jahn-Teller mediated lattice distortion depleted the DOS at E_F by one-third, it is large enough not to stabilize the system in a nonmagnetic ground state. However, the depletion of the DOS at E_F through the spin polarization opens up a gap at E_F by pushing the spin-up bands below and spin-down bands above in energy, as shown in Fig. 2. With one unoccupied spin minority band for each Cu, the system gives rise to a spin-1/2 lattice. From our total energy calculations on several spin arrangements of this spin-1/2 lattice, we find that the G -type antiferromagnetic ordering forms the ground state. The partial DOS for the latter is depicted in Fig. 5 and will be discussed later. Further understanding of the magnetization of this compound is obtained by calculating the magnetic exchange interactions, which are discussed next.

B. Exchange interactions for the d^0 system

To find the underlying mechanism governing the magnetic ordering in this system, a detailed study of spin-exchange interactions is necessary. In one of the works by Toyoda *et al.* [26], the exchange interactions J_1 , J_2 , and J_3 (see Fig. 3)

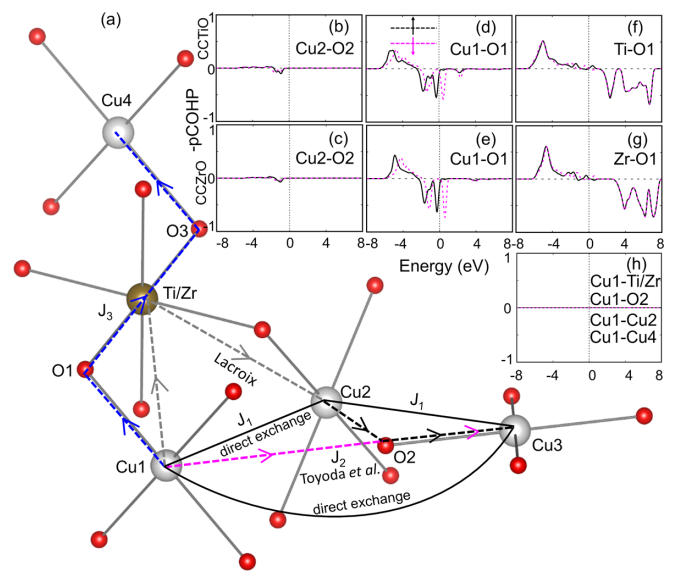


FIG. 3. (a) Depiction of exchange interaction paths for J_1 , J_2 , and J_3 . (b)–(h) The pCOHP of various atom pairs in CCTiO and CCZrO. The negative (positive) values of pCOHP indicate the antibonding (bonding) states, respectively.

were explained with the aid of a classical Heisenberg Hamiltonian, cluster model, and charge density analysis. J_1 and J_2 are found to be weakly ferromagnetic and indirect, mediated by the superexchange mechanism via the Cu-O-Cu path as depicted through Fig. 3(a). Contrary to J_1 and J_2 , the J_3 was found to be strong and antiferromagnetic ($J_3 \approx 5J_1$ and $J_3 \approx 5J_2$), mediated by long-range superexchange interaction via the Cu-O-Ti-O-Cu path. Even though the nature of magnetic couplings was similar for both CCTiO and CCZrO, the cause for the higher strength of J_3 in the former has not been discussed in this work. Furthermore, the estimated value of T_N (≈ 70 K) for CCTiO is nearly three times higher than the experimentally reported value of ≈ 25 K [15].

In another study on CCTiO by Lacroix, a perturbative Hamiltonian approach was adopted to propose that the exchange paths are defined through Cu-Ti-Cu interactions [see Fig. 3(a)] [27]. The G -type magnetic structure was interpreted by considering the competition between superexchange interaction and spin anisotropy. Though the absolute value of the exchange interaction strengths was not determined, the J_3 was estimated to be 10 times higher than J_1 and J_2 .

The aforementioned discussion suggests that an intricate analysis of the magnetic coupling is needed to determine the appropriate mechanism that stabilizes the G -type magnetic ordering as well as to accurately estimate T_N for this system. For this purpose, we have employed Noodelmann's broken-symmetry spin dimer method [42] on CCTiO and CCZrO. In this method, the energy difference between high spin (HS) and broken symmetry (BS) configurations is given by

$$E_{HS} - E_{BS} = \frac{1}{2} S_{\max}^2 J, \quad (2)$$

where J is related to the spin-dimer Hamiltonian $H = \sum_{i<j} J_{ij} S_i S_j$, and S_{\max} is the maximum number of unoccupied spins of the dimer. For the present case, each monomer has one unoccupied spin, hence the above equation can be expressed as

$$E_{HS} - E_{BS} = \frac{J}{2}. \quad (3)$$

E_{HS} and E_{BS} are evaluated by performing the DFT calculations for HS and BS configurations, respectively. To evaluate the J_i 's strength, four different magnetic configurations, namely FM, A-type, G -type, and AFM3, are considered and are shown in Figs. 4(a)–4(d). Using the spin-dimer Hamiltonian for these magnetic configurations, we have evaluated the spin-exchange energies (per f.u.) in terms of the exchange parameters, and they are expressed as

$$\begin{aligned} E_{\text{FM}} &= \frac{1}{8}(12J_1 + 24J_2 + 24J_3), \\ E_{\text{A-AFM}} &= \frac{1}{8}(4J_1 - 8J_2 - 24J_3), \\ E_{\text{G-AFM}} &= \frac{1}{8}(-12J_1 + 24J_2 - 24J_3), \\ E_{\text{AFM3}} &= \frac{1}{8}(-4J_1 - 8J_2 + 8J_3). \end{aligned} \quad (4)$$

These spin-exchange energies are mapped to the total energy obtained from the DFT calculations for the respective magnetic configuration. Further, using Eq. (2), the J values are estimated as a function of U for both experimental and optimized crystal structures of CCTiO. For CCZrO the exchange parameters are calculated only for the optimized structure as

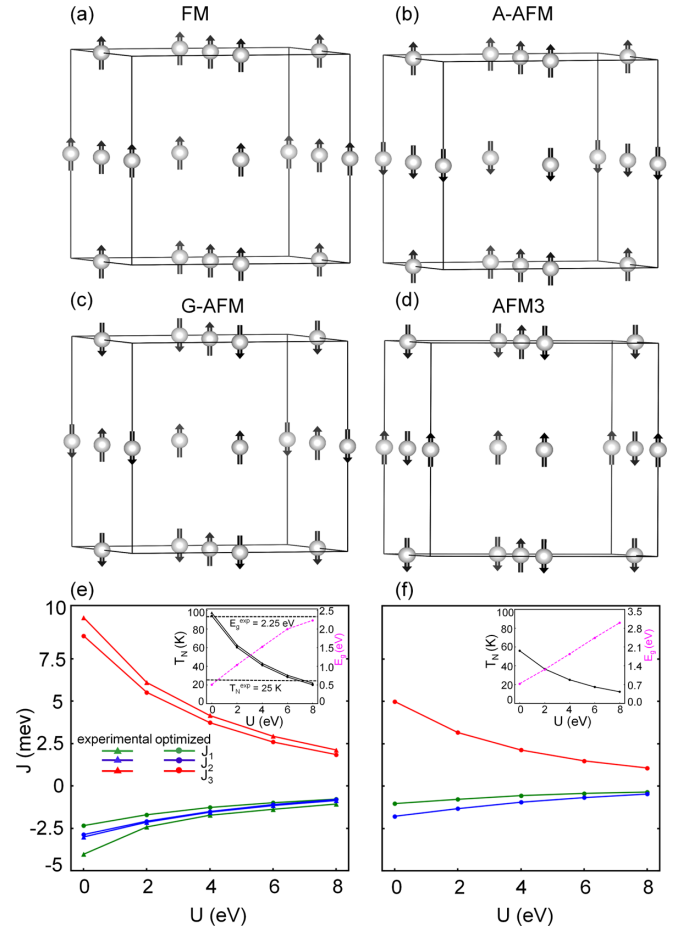


FIG. 4. (a)–(d) The magnetic configurations, namely, FM, A-AFM, G -AFM, and AFM-3. (e),(f) The variation of exchange couplings J_1 , J_2 , J_3 , and Néel temperature T_N with U (see the inset) for experimental and optimized structures of CCTiO and CCZrO. The dashed lines represent the experimentally obtained values of T_N and E_g , respectively.

it has yet to be experimentally synthesized. Further, the Néel temperature was estimated using Eq. (5), where Θ_{CW} , K_B , Z_i , and μ represent the Curie-Weiss temperature, the Boltzmann constant, the coordination number corresponding to each J_i interaction, and the mean-field constant, respectively, and the results are shown in Fig. 4. For CCTiO, we have considered $\mu = \frac{\Theta_{\text{CW}}}{T_N}$ ($= 1.30$) as reported in one of the experimental works [10]. However, the CCZrO has yet to be experimentally synthesized. Therefore, for CCZrO, the μ value is taken as that of CCTiO. This value of μ is fair enough to consider as both the former and the latter adopt the same structural framework, and both Zr and Ti have a d^0 electronic configuration. Here, the positive (negative) values of J indicate AFM (FM) coupling between neighboring spins. As expected, J_1 and J_2 are weak and ferromagnetically coupled, whereas J_3 is antiferromagnetic. Keeping these modes of interactions intact, we found the conditions to stabilize different magnetic ordering in these systems, and they are listed in Table II.

To identify the correct spin-exchange pathways, the bonding strength between various atom pairs is calculated using COHP, and the results are shown in Figs. 3(b)–3(h). The J_1

TABLE II. The conditions for the stabilization of G -AFM, FM, A-AFM, and AFM3 magnetic configurations. These conditions are obtained from Eq. (4) and by considering that J_1, J_2 are weak and ferromagnetically coupled, and J_3 is antiferromagnetically coupled (see the main text).

Magnetic configurations	Conditions (in absolute values of J_i)
G -AFM	$J_1 < 2J_2, J_1 < 2J_3$
FM	$J_1 > 2J_3, J_2 > J_3$
A-AFM	$J_1 > 2J_2, J_3 > 4J_2$
AFM3	$J_1 > 4J_3, J_3 > J_2$

and J_2 paths adopted by Toyoda *et al.* include intermediate oxygen atoms through Cu2-O2-Cu3 $pd\pi$ and Cu1-O2-Cu3 $pd\sigma$ covalent interactions, respectively [see Fig. 3(a)]. However, the COHP calculations suggest that Cu1-O2 and Cu2-O2 atom pairs hardly have any covalent bonding. Hence, such indirect exchange pathways are least probable. As discussed earlier, Lacroix considered the Cu-Ti-Cu path for both J_1 and J_2 and explained the strength through a Cu-Ti electron transfer integral. However, the COHP result shown in Fig. 3(h) predicts the Cu1-Ti interaction to be zero, and hence such indirect exchange pathways are improbable. Furthermore, the nearest and next-nearest CuO₄ square planar complexes, and thereby the Cu- d orbitals occupying the unpaired electrons, are orthogonal to each other. Therefore, the overlapping of these orbitals in the nearest and next-nearest neighborhood is negligible. This implies that J_1 and J_2 are mediated through a direct exchange mechanism. Similar inferences are obtained for CCZrO.

The third-neighbor CuO₄ complexes are nonorthogonal. However, due to a large separation between Cu1 and Cu4 ions, the hybridization between Cu- d orbitals is negligible. Since the direct exchange operates for short internuclear separations, J_3 can only be explained through indirect exchange mechanisms. The COHP for Cu1-O1 and Ti/Zr-O1 pairs, plotted in Figs. 3(d)–3(g), shows a stronger overlap among the orbitals of these pairs. Furthermore, since the bonding states (antibonding states) corresponding to Cu1-O1, O1-Ti/Zr, Ti/Zr-O3, and O3-Cu4 pairs are in almost the same energy level, the electron transfer across them becomes easier and thereby the indirect exchange path is favored. This is in agreement with Tyoda *et al.*, who have predicted indirect superexchange mediated antiferromagnetic interaction along this path,

$$\Theta_{\text{CW}} = -\frac{S(S+1)}{3K_B} \sum_i Z_i J_i, \quad T_N = \frac{|\Theta_{\text{CW}}|}{\mu}. \quad (5)$$

The relative strength of J_1, J_2 , and J_3 as obtained in this mean-field study within the framework of the GGA implies the stabilization of the G -type ordering. However, the T_N estimated using Eq. (4) is found to be ≈ 95 K, which is approximately four times the experimentally observed T_N value, which is an expected overestimation in the mean-field framework. In the following section, we will see that this can be addressed by taking into account the electron correlation effect.

IV. ROLE OF ON-SITE COULOMB REPULSION AND LATTICE DISTORTIONS ON MAGNETISM

The effect of strong correlation on the electronic structure of CCTiO and CCZrO is analyzed through DFT+ U calculations. In Fig. 5 we have plotted the orbital- and spin-resolved DOS for CCTiO and CCZrO as a function of U . As Ti/Zr exhibits a d^0 electronic configuration, the Ti/Zr d states reside in the conduction band and are inactive. For CCZrO, the Zr- d states are located far above the E_F relative to the CCTiO. As was already discussed, the system exhibits a band gap through magnetization even in the absence of on-site Coulomb repulsion. Increasing the strength of U localizes the Cu- d states and pushes the valence and conduction band apart to widen the band gap. The localization reduces the strength of covalent interactions and therefore it influences the indirect exchange interaction significantly. This can be observed from Fig. 4(e) and Fig. 4(f), where the strength of J_1, J_2 , and J_3 are plotted as a function of U for CCTiO and CCZrO respectively. Qualitatively one can express the magnetic exchange interaction between two states $|m\rangle$ and $|m'\rangle$ as $J_{\text{eff}}(i \rightarrow j) = f(t_{mm'}, U) - \langle m|V_{ij}|m'\rangle_{\text{exch}}$ [43]. Herein, the states $|m\rangle$ and $|m'\rangle$ represent the valence orbitals of Cu²⁺ ions at lattice sites i and j , and V_{ij} is the Coulomb interaction between the former and the latter. In the first term, $t_{mm'}$ denotes the effective hopping integral (direct or indirect), and the function f depends on the number of intermediate paths connecting $|m\rangle$ and $|m'\rangle$. The second term is the direct exchange interaction. This further validates the fact that J_1 and J_2 are direct exchange interactions while J_3 is indirect. For J_1 and J_2 , the first term vanishes due to the orthogonality of the Cu- d orbitals and hence only the second term contributes, which is independent of the on-site Coulomb repulsion as also inferred from Figs. 4(e) and 4(f). For J_3 , the first term dominates and as a result J_3 decays rapidly with increasing on-site Coulomb repulsion U .

Figures 4(e) and 4(f) enable us to calculate T_N as a function of U for CCTiO and CCZrO, respectively, and the results are shown in the insets. For CCTiO, the theoretical estimation of T_N and the band gap (E_g) matches with the experimental one for $U \approx 7$ and 8 eV, respectively [44]. Therefore, the strength of U lies in the range of 7–8 eV, signifying that these systems are strongly correlated. For $U = 7$ eV, we predict the T_N of CCZrO to be ≈ 15 K. In the case of CCTiO, we find that the exchange interaction strengths for the optimized structure vary little with that of the experimental structure [see Fig. 4(e)]. Therefore, the predicted T_N is expected to match with the experimental value for yet to be synthesized CCZrO. Often strain and pressure are used to tune the magnetic properties of correlated oxides in general and perovskites in particular [45–48]. To examine if these are critical factors in the case of CCTiO and CCZrO, we estimated the J_i 's and hence T_N as a function of strain and pressure. While the G -AFM ordering remains robust within $\pm 2\%$ strain and pressure, T_N was found to be tunable by 10 and 5 K for CCTiO and CCZrO, respectively (see Table III).

Based on the qualitative arguments made above in the previous paragraphs, it is expected that $|J_1|$ with a shorter exchange path is greater than $|J_2|$. While it is true for the experimentally obtained crystal structure of CCTiO, the same

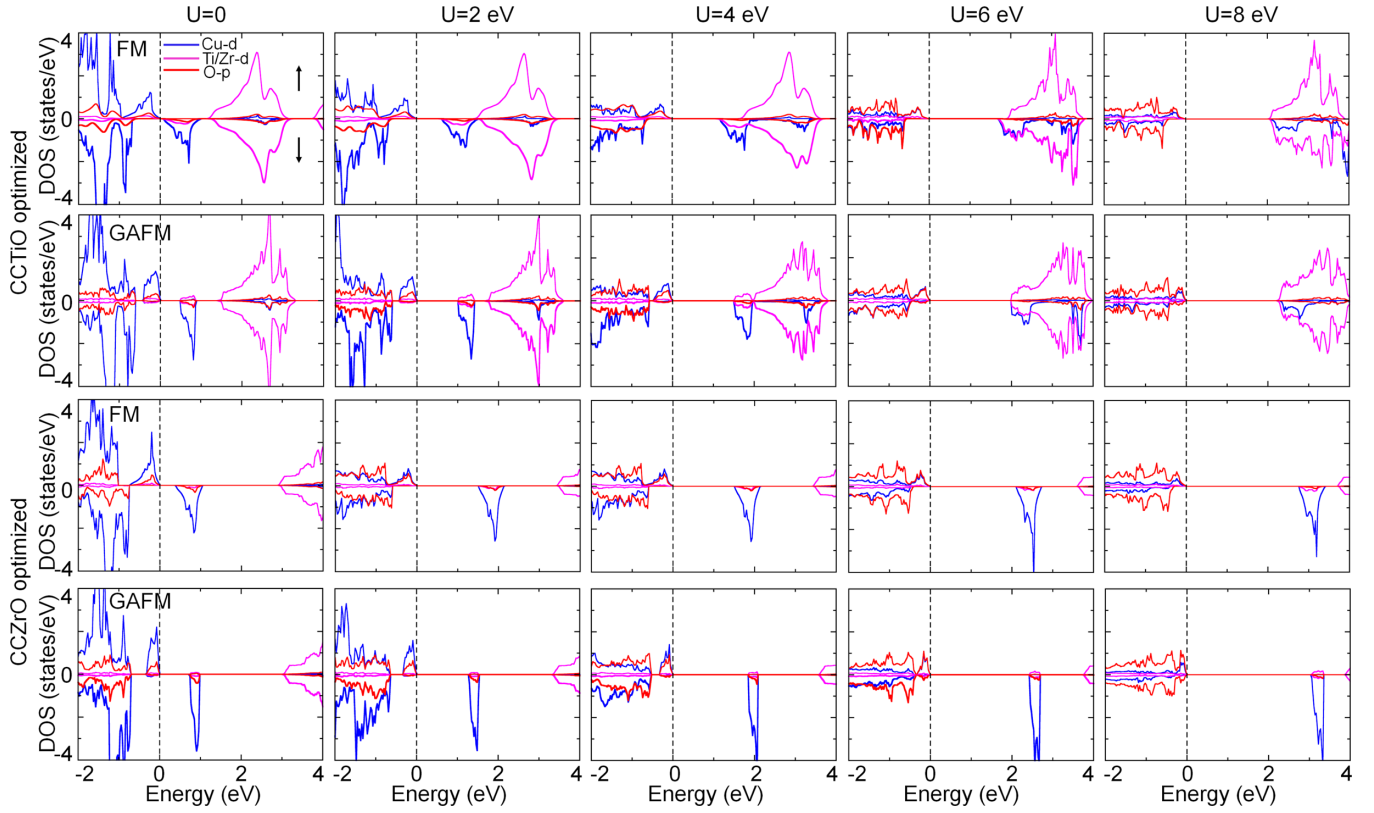


FIG. 5. The projected density of states of FM and *G*-AFM states as a function of U for optimized CCTiO (first and second row) and CCZrO (third and fourth row). The up and down arrows represent the spin-up and spin-down channels. The Fermi energy is set at zero.

cannot be said for the optimized structure. This suggests that there is an additional term in V_{ij} other than the dominant $1/|r_{ij}|$ term, and the states $|m\rangle$ and $|m'\rangle$ may not be completely orthogonal. This needs further investigation. We would also like to further note that at higher values of U_{eff} , say 7 eV, at which the estimated T_N agrees well with the experimental value, both J_1 and J_2 converge to <1 meV. Therefore, the qualitative inference and conclusions in this study are not affected by the error associated with the comparative estimation of J_1 and J_2 .

V. SUMMARY

To summarize, with the aid of density functional calculations, phonon studies, and spin dimer analysis, we have examined the structural stability and the electronic and magnetic structures of *A*-site ordered perovskites CCTiO and CCZrO. We show that the symmetry lowered transition from

regular perovskite structure to *A*-site ordered perovskite structure is driven by Jahn-Teller distortion, where a CuO_{12} icosahedron gives rise to a CuO_4 square-planar complex. The underlying mechanism that stabilizes the experimentally observed *G*-type antiferromagnetic ordering of the Cu spin-1/2 lattice is explained by calculating nearest, next-nearest, and third-nearest exchange paths. By analyzing the crystal orbital Hamiltonian population, we established that the nearest and next-nearest exchange interactions are direct and weakly ferromagnetic, and the third neighbor is indirect and strongly antiferromagnetic. The stabilization of *G*-AFM ordering is due to the fact that the strength of J_3 is greater than half of J_1 . This addresses the ambiguities on the nature of exchange interactions reported in the literature. The correlation effect has a major role in determining the Néel temperature. By pursuing DFT+ U calculations, we show that the experimental and theoretical values of T_N agree well for $U \approx 7$ eV. Furthermore, we show that the magnetization and spin arrangements are robust against pressure and strain.

As a whole, we believe that the present study will pave the way to revisit the electronic and magnetic structure of other members of the *A*-site ordered perovskite family.

ACKNOWLEDGMENTS

The authors would like to thank HPCE, IIT Madras for providing the computational facility. B.R.K.N. would like to thank Debakanta Samal for fruitful discussions. This work is funded by the Department of Science and Technology, India, through Grant No. CRG/2020/004330.

TABLE III. The T_N (in K) of optimized CCTiO and CCZrO corresponding to 2% uniform compression, expansion, and 2% epitaxial tensile strain with U as 7 eV. The T_N of equilibrium structure is also provided for comparison.

External stimuli	CCTiO	CCZrO
Uniform compression	29.75	17.16
Equilibrium structure	25	15
Uniform expansion	19.41	11.99
Epitaxial tensile strain	23.10	14.13

- [1] E. O. Wollan and W. C. Koehler, *Phys. Rev.* **100**, 545 (1955).
- [2] H. Y. Hwang, T. T. M. Palstra, S.-W. Cheong, and B. Batlogg, *Phys. Rev. B* **52**, 15046 (1995).
- [3] N. Ramadass, *Mater. Sci. Eng.* **36**, 231 (1978).
- [4] P. Ravindran, P. A. Korzhavyi, H. Fjellvåg, and A. Kjekshus, *Phys. Rev. B* **60**, 16423 (1999).
- [5] D. Fuchs, E. Arac, C. Pinta, S. Schuppler, R. Schneider, and H. v. Löhneysen, *Phys. Rev. B* **77**, 014434 (2008).
- [6] A. Vailionis, H. Boschker, W. Siemons, E. P. Houwman, D. H. A. Blank, G. Rijnders, and G. Koster, *Phys. Rev. B* **83**, 064101 (2011).
- [7] J. Varignon, N. C. Bristowe, and P. Ghosez, *Phys. Rev. Lett.* **116**, 057602 (2016).
- [8] A. Chauhan and B. R. K. Nanda, *Phys. Rev. B* **105**, 045127 (2021).
- [9] A. Chauhan and B. R. K. Nanda, *Appl. Phys. Lett.* **119**, 261906 (2021).
- [10] Y. Shimakawa, *Inorg. Chem.* **47**, 8562 (2008).
- [11] I. Yamada, Y. Takahashi, K. Ohgushi, N. Nishiyama, R. Takahashi, K. Wada, T. Kunimoto, H. Ohfuji, Y. Kojima, T. Inoue, and T. Irifune, *Inorg. Chem.* **49**, 6778 (2010).
- [12] M. A. Subramanian, D. Li, N. Duan, B. A. Reisner, and A. W. Sleight, *J. Solid State Chem.* **151**, 323 (2000).
- [13] C. McGuinness, J. E. Downes, P. Sheridan, P.-A. Glans, K. E. Smith, W. Si, and P. D. Johnson, *Phys. Rev. B* **71**, 195111 (2005).
- [14] Y. Lin, Y. B. Chen, T. Garret, S. W. Liu, C. L. Chen, L. Chen, R. P. Bontchev, A. Jacobson, J. C. Jiang, E. I. Meletis, J. Horwitz, and H.-D. Wu, *Appl. Phys. Lett.* **81**, 631 (2002).
- [15] A. Koitzsch, G. Blumberg, A. Gozar, B. Dennis, A. P. Ramirez, S. Trebst, and S. Wakimoto, *Phys. Rev. B* **65**, 052406 (2002).
- [16] Y. Kim, S. Wakimoto, S. Shapiro, P. Gehring, and A. Ramirez, *Solid State Commun.* **121**, 625 (2002).
- [17] M. Mizumaki, T. Saito, H. Shiraki, and Y. Shimakawa, *Inorg. Chem.* **48**, 3499 (2009).
- [18] Z. Zeng, M. Greenblatt, M. A. Subramanian, and M. Croft, *Phys. Rev. Lett.* **82**, 3164 (1999).
- [19] X. Hao, Y. Xu, F. Gao, D. Zhou, and J. Meng, *Phys. Rev. B* **79**, 113101 (2009).
- [20] D. Meyers, S. Mukherjee, J. G. Cheng, S. Middey, J. S. Zhou, J. B. Goodenough, B. A. Gray, J. W. Freeland, T. Saha-Dasgupta, and J. Chakhalian, *Sci. Rep.* **3**, 1834 (2013).
- [21] S. Lv, X. Liu, H. Li, D. Han, and J. Meng, *J. Phys. Chem. C* **115**, 2366 (2011).
- [22] I. Yamada, M. Ochi, M. Mizumaki, A. Hariki, T. Uozumi, R. Takahashi, and T. Irifune, *Inorg. Chem.* **53**, 7089 (2014).
- [23] S. Hébert, R. Daou, and A. Maignan, *Phys. Rev. B* **91**, 045106 (2015).
- [24] S. Jana, S. G. Bhat, B. C. Behera, L. Patra, P. S. Anil Kumar, B. R. K. Nanda, and D. Samal, *Europhys. Lett.* **133**, 17005 (2021).
- [25] H. Shiraki, T. Saito, T. Yamada, M. Tsujimoto, M. Azuma, H. Kurata, S. Isoda, M. Takano, and Y. Shimakawa, *Phys. Rev. B* **76**, 140403(R) (2007).
- [26] M. Toyoda, K. Yamauchi, and T. Oguchi, *Phys. Rev. B* **87**, 224430 (2013).
- [27] C. Lacroix, *J. Phys. C* **13**, 5125 (1980).
- [28] P. Lunkenheimer, R. Fichtl, S. G. Ebbinghaus, and A. Loidl, *Phys. Rev. B* **70**, 172102 (2004).
- [29] J.-C. Zheng, A. I. Frenkel, L. Wu, J. Hanson, W. Ku, E. S. Božin, S. J. L. Billinge, and Y. Zhu, *Phys. Rev. B* **81**, 144203 (2010).
- [30] D. R. Hamann, *Phys. Rev. Lett.* **42**, 662 (1979).
- [31] P. Blaha, K. Schwartz, G. Madsen, D. Kvasnicka, and J. Luitz, *WIEN2k An Augmented Plane Wave+Local Orbitals Program for Calculating Crystal Properties* (Karlheinz Schwartz, Tech. Universitt Wien, Austria, 2001).
- [32] S. L. Dudarev, G. A. Botton, S. Y. Savrasov, C. J. Humphreys, and A. P. Sutton, *Phys. Rev. B* **57**, 1505 (1998).
- [33] V. I. Anisimov and O. Gunnarsson, *Phys. Rev. B* **43**, 7570 (1991).
- [34] P. Giannozzi, S. de Gironcoli, P. Pavone, and S. Baroni, *Phys. Rev. B* **43**, 7231 (1991).
- [35] X. Gonze and C. Lee, *Phys. Rev. B* **55**, 10355 (1997).
- [36] A. Togo, L. Chaput, I. Tanaka, and G. Hug, *Phys. Rev. B* **81**, 174301 (2010).
- [37] A. Togo, F. Oba, and I. Tanaka, *Phys. Rev. B* **78**, 134106 (2008).
- [38] R. Dronskowski and P. E. Bloechl, *J. Phys. Chem.* **97**, 8617 (1993).
- [39] V. L. Deringer, A. L. Tchougréeff, *J. Phys. Chem. A* **115**, 5461 (2011).
- [40] H. A. Jahn and E. Teller, *Proc. R. Soc. London A* **161**, 220 (1937).
- [41] P. Parida, R. Kashikar, A. Jena, and B. R. K. Nanda, *J. Phys. Chem. Solids* **123**, 133 (2018).
- [42] L. Noodleman, *J. Chem. Phys.* **74**, 5737 (1981).
- [43] K. Yosida, *Theory of Magnetism* (Springer-Verlag, New York, 1998).
- [44] X. Huang, H. Zhang, M. Wei, Y. Lai, and J. Li, *J. Alloys Compd.* **708**, 1026 (2017).
- [45] B. R. K. Nanda and S. Satpathy, *Phys. Rev. B* **80**, 165430 (2009).
- [46] A. Marthinsen, C. Faber, U. Aschauer, N. A. Spaldin, and S. M. Selbach, *MRS Commun.* **6**, 182(2016).
- [47] B. R. K. Nanda and S. Satpathy, *Phys. Rev. B* **81**, 174423 (2010).
- [48] D. Meng, H. Guo, Z. Cui, C. Ma, J. Zhao, J. Lu, H. Xu, Z. Wang, X. Hu, Z. Fu, R. Peng, J. Guo, X. Zhai, G. J. Brown, R. Knize, and Y. Lu, *Proc. R. Soc. London A* **115**, 2873 (2018).